



**HAL**  
open science

## Large heterogeneities in comet 67P as revealed by active pits from sinkhole collapse

Jean-Baptiste Vincent, Dennis Bodewits, Sébastien Besse, Holger Sierks, Cesare Barbieri, Philippe Lamy, Rafael Rodrigo, Detlef Koschny, Hans Rickman, Horst Uwe Keller, et al.

### ► To cite this version:

Jean-Baptiste Vincent, Dennis Bodewits, Sébastien Besse, Holger Sierks, Cesare Barbieri, et al.. Large heterogeneities in comet 67P as revealed by active pits from sinkhole collapse. *Nature*, 2015, 523 (7558), pp.63-66. 10.1038/nature14564. insu-01176031

**HAL Id: insu-01176031**

**<https://insu.hal.science/insu-01176031>**

Submitted on 8 Nov 2022

**HAL** is a multi-disciplinary open access archive for the deposit and dissemination of scientific research documents, whether they are published or not. The documents may come from teaching and research institutions in France or abroad, or from public or private research centers.

L'archive ouverte pluridisciplinaire **HAL**, est destinée au dépôt et à la diffusion de documents scientifiques de niveau recherche, publiés ou non, émanant des établissements d'enseignement et de recherche français ou étrangers, des laboratoires publics ou privés.

# Large heterogeneities in comet 67P as revealed by active pits from sinkhole collapse

Jean-Baptiste Vincent<sup>1</sup>, Dennis Bodewits<sup>2</sup>, Sébastien Besse<sup>3</sup>, Holger Sierks<sup>1</sup>, Cesare Barbieri<sup>4</sup>, Philippe Lamy<sup>5</sup>, Rafael Rodrigo<sup>6,7</sup>, Detlef Koschny<sup>3</sup>, Hans Rickman<sup>8,9</sup>, Horst Uwe Keller<sup>10</sup>, Jessica Agarwal<sup>1</sup>, Michael F. A'Hearn<sup>2,11</sup>, Anne-Thérèse Auger<sup>5</sup>, M. Antonella Barucci<sup>12</sup>, Jean-Loup Bertaux<sup>13</sup>, Ivano Bertini<sup>14</sup>, Claire Capanna<sup>5</sup>, Gabriele Cremonese<sup>15</sup>, Vania Da Deppo<sup>16</sup>, Björn Davidsson<sup>6</sup>, Stefano Debei<sup>17</sup>, Mariolino De Cecco<sup>18</sup>, Mohamed Ramy El-Maarry<sup>19</sup>, Francesca Ferri<sup>14</sup>, Sonia Fornasier<sup>12</sup>, Marco Fulle<sup>20</sup>, Robert Gaskell<sup>21</sup>, Lorenza Giacomini<sup>14</sup>, Olivier Groussin<sup>5</sup>, Aurélie Guilbert-Lepoutre<sup>2</sup>, P. Gutierrez-Marques<sup>1</sup>, Pedro J. Gutiérrez<sup>22</sup>, Carsten Güttler<sup>1</sup>, Nick Hoekzema<sup>1</sup>, Sebastian Höfner<sup>1</sup>, Stubbe F. Hviid<sup>23</sup>, Wing-Huen Ip<sup>24</sup>, Laurent Jorda<sup>5</sup>, Jörg Knollenberg<sup>23</sup>, Gabor Kovacs<sup>1</sup>, Rainer Kramm<sup>1</sup>, Ekkehard Kührt<sup>23</sup>, Michael Küppers<sup>25</sup>, Fiorangela La Forgia<sup>4</sup>, Luisa M. Lara<sup>22</sup>, Monica Lazzarin<sup>4</sup>, Vicky Lee<sup>24</sup>, Cédric Leyrat<sup>12</sup>, Zhong-Yi Lin<sup>24</sup>, José J. Lopez Moreno<sup>22</sup>, Stephen Lowry<sup>26</sup>, Sara Magrin<sup>27</sup>, Lucie Maquet<sup>25</sup>, Simone Marchi<sup>28</sup>, Francesco Marzari<sup>27</sup>, Matteo Massironi<sup>29</sup>, Harald Michalik<sup>30</sup>, Richard Moissl<sup>25</sup>, Stefano Mottola<sup>23</sup>, Giampiero Naletto<sup>14,16,31</sup>, Nilda Oklay<sup>1</sup>, Maurizio Pajola<sup>14</sup>, Frank Preusker<sup>23</sup>, Frank Scholten<sup>23</sup>, Nicolas Thomas<sup>19</sup>, Imre Toth<sup>32</sup> & Cecilia Tubiana<sup>1</sup>

**Pits have been observed on many cometary nuclei mapped by spacecraft<sup>1-4</sup>. It has been argued that cometary pits are a signature of endogenic activity, rather than impact craters such as those on planetary and asteroid surfaces. Impact experiments<sup>5,6</sup> and models<sup>7,8</sup> cannot reproduce the shapes of most of the observed cometary pits, and the predicted collision rates imply that few of the pits are related to impacts<sup>8,9</sup>. Alternative mechanisms like explosive activity<sup>10</sup> have been suggested, but the driving process remains unknown. Here we report that pits on comet 67P/Churyumov–Gerasimenko are active, and probably created by a sinkhole process, possibly accompanied by outbursts. We argue that after formation, pits expand slowly in diameter, owing to sublimation-driven retreat of the walls. Therefore, pits characterize how eroded the surface is: a fresh cometary surface will have a ragged structure with many pits, while an evolved surface will look smoother. The size and spatial distribution of pits imply that large heterogeneities exist in the physical, structural or compositional properties of the first few hundred metres below the current nucleus surface.**

Understanding the differences in local activity of comet nuclei helps us to constrain how their surfaces have evolved since their formation. From July to December 2014, the OSIRIS (Optical, Spectroscopic, and Infrared Remote Imaging System) cameras on board Rosetta<sup>11</sup> continuously monitored the activity of comet 67P/Churyumov–Gerasimenko (referred to, hereafter, as comet 67P) from about a 30 km distance from the surface of the nucleus and resolved the fine structure of dust jets<sup>12</sup>. By means of stereo reconstruction, we found that broad jets can be separated into narrower features, which are linked unambiguously to

quasi-circular depressions and to walls of alcoves that are a few tens to a few hundreds of metres in diameter. These pits are remarkably symmetric and similar in size, and show interesting morphological details such as horizontal layers and terraces, vertical striations, and a smooth floor seemingly covered with dust. Some of these pits are as deep as a few hundred metres and provide a glimpse well below the nucleus surface. We detected a set of 18 quasi-circular pits on the northern hemisphere of comet 67P (Extended Data Table 1, Fig. 1). We observed that pits tend to cluster in small groups, and that several pits are active (Fig. 2). We measured the depth-to-diameter ratio ( $d/D$ ) of the pits and found that active pits have a high  $d/D = 0.73 \pm 0.08$ , while pits that are currently inactive are much shallower with mean  $d/D = 0.26 \pm 0.08$  (Extended Data Table 1, Fig. 3). The  $d/D$  ratio of these active pits is much higher than that of circular depressions on other comets:  $d/D = 0.1$  on comet 9P/Tempel 1 (ref. 4), and  $d/D = 0.2$  on comet 81P/Wild 2 (refs 13 and 14).

The difference in pit morphology on the three comets may reflect their different histories. For Jupiter family comets, the time since the last encounter with Jupiter is a proxy for the thermal history of the surface. Comet 9P is considered to be more processed by sublimation than comet 81P (ref. 3). In that view, comet 67P is relatively unprocessed by sublimation because its perihelion was brought from 2.7 astronomical units (AU) to 1.2 AU by a close encounter with Jupiter in 1959 (see Methods subsection ‘Orbit integration’). Comet 81P is also considered a young comet, but its pitted terrains are exposed to the Sun at perihelion and so have experienced much stronger erosion than the pitted areas on comet 67P even though it has spent less time in the

<sup>1</sup>Max-Planck-Institut für Sonnensystemforschung, Justus-von-Liebig-Weg 3, 37077 Göttingen, Germany. <sup>2</sup>University of Maryland, Department of Astronomy, College Park, Maryland 20742-2421, USA. <sup>3</sup>Scientific Support Office, European Space Research and Technology Centre/ESA, Keplerlaan 1, Postbus 299, 2201 AZ Noordwijk ZH, The Netherlands. <sup>4</sup>University of Padova, Department of Physics and Astronomy, Vicolo dell’Osservatorio 3, 35122 Padova, Italy. <sup>5</sup>Laboratoire d’Astrophysique de Marseille, UMR 7326, CNRS and Aix Marseille Université, 13388 Marseille Cedex 13, France. <sup>6</sup>Centro de Astrobiología, CSIC-INTA, 28850 Torrejón de Ardoz, Madrid, Spain. <sup>7</sup>International Space Science Institute, Hallerstraße 6, 3012 Bern, Switzerland. <sup>8</sup>Department of Physics and Astronomy, Uppsala University, Box 516, 75120 Uppsala, Sweden. <sup>9</sup>PAS Space Research Center, Bartycka 18A, 00716 Warszawa, Poland. <sup>10</sup>Institut für Geophysik und extraterrestrische Physik (IGEP), Technische Universität Braunschweig, Mendelssohnstraße 3, 38106 Braunschweig, Germany. <sup>11</sup>Akademie der Wissenschaften zu Göttingen and Max-Planck-Institut für Sonnensystemforschung, Justus-von-Liebig-Weg 3, 37077 Göttingen, Germany. <sup>12</sup>LESIA-Observatoire de Paris, CNRS, Université Pierre et Marie Curie, Université Paris Diderot, 5 place Jules Janssen, 92195 Meudon, France. <sup>13</sup>LATMOS, CNRS/UVSQ/IPSL, 11 boulevard d’Alembert, 78280 Guyancourt, France. <sup>14</sup>Centro di Ateneo di Studi ed Attività Spaziali “Giuseppe Colombo” (CISAS), University of Padova, via Venezia 15, 35131 Padova, Italy. <sup>15</sup>INAF, Osservatorio Astronomico di Padova, Vicolo dell’Osservatorio 5, 35122 Padova, Italy. <sup>16</sup>CNR-IFN UOS Padova LUXOR, via Trasea 7, 35131 Padova, Italy. <sup>17</sup>Department of Industrial Engineering, University of Padova, via Venezia 1, 35131 Padova, Italy. <sup>18</sup>University of Trento, via Mesiano 77, 38100 Trento, Italy. <sup>19</sup>Physikalisches Institut der Universität Bern, Sidlerstraße 5, 3012 Bern, Switzerland. <sup>20</sup>INAF Osservatorio Astronomico, via Tiepolo 11, 34014 Trieste, Italy. <sup>21</sup>Planetary Science Institute, Tucson, Arizona 85719, USA. <sup>22</sup>Instituto de Astrofísica de Andalucía (CSIC), Glorieta de la Astronomía s/n, 18008 Granada, Spain. <sup>23</sup>Deutsches Zentrum für Luft- und Raumfahrt (DLR), Institut für Planetenforschung, Rutherfordstraße 2, 12489 Berlin, Germany. <sup>24</sup>National Central University, Graduate Institute of Astronomy, 300 Chung-Da Rd, Chung-Li 32054, Taiwan. <sup>25</sup>Operations Department, European Space Astronomy Centre/ESA, PO Box 78, 28691 Villanueva de la Canada, Madrid, Spain. <sup>26</sup>The University of Kent, School of Physical Sciences, Canterbury, Kent CT2 7NZ, UK. <sup>27</sup>University of Padova, Department of Physics and Astronomy, via Marzolo 8, 35131 Padova, Italy. <sup>28</sup>Solar System Exploration Research Virtual Institute, Southwest Research Institute, 1050 Walnut Street, Suite 300, Boulder, Colorado 80302, USA. <sup>29</sup>Dipartimento di Geoscienze, University of Padova, via Giovanni Gradenigo 6, 35131 Padova, Italy. <sup>30</sup>Institut für Datentechnik und Kommunikationsnetze der Technische Universität Braunschweig, Hans-Sommer-Straße 66, 38106 Braunschweig, Germany. <sup>31</sup>University of Padova, Department of Information Engineering, via Gradenigo 6/B, 35131 Padova, Italy. <sup>32</sup>Konkoly Observatory of the Hungarian Academy of Sciences, PO Box 67, 1525 Budapest, Hungary.

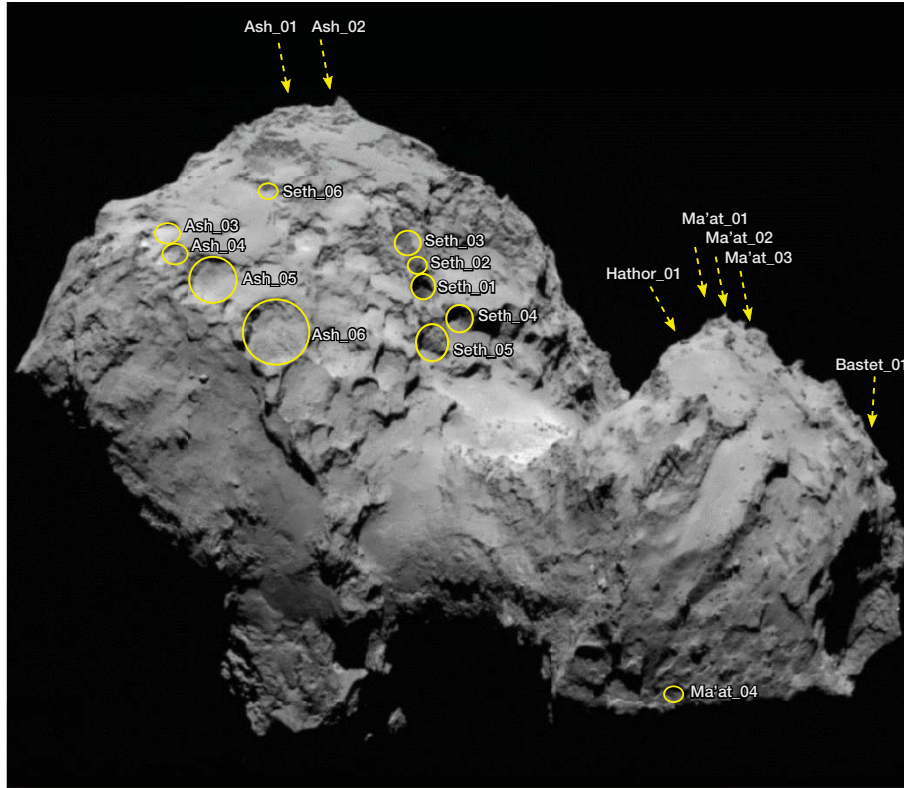


**Figure 1 | Location of the pits considered in this study.** A non-exhaustive catalogue of depressions sharing similar morphologies to those unambiguously linked to jets in the Seth and Ma'at regions.

inner Solar System. Deep active pits on comets are seemingly found preferentially on surfaces that have not been notably eroded.

The terrain morphology inside the pits on comet 67P is not uniform and is classified as: very smooth texture; fractured terrain, terraces and alcoves; or globular texture. The globular texture is detected only in the deep pits and at a few additional locations on the nucleus, where deeper near-surface layers can be observed. This morphology extends to a depth of at least 200m below the current nucleus surface (see, for example, pit Seth\_01, Extended Data Fig. 2).

Jets arise from the edges of active pits, primarily from heavily fractured and globular morphologies (Fig. 2). However, the  $d/D$  ratio cannot be explained by current sublimation-driven retreat of the walls. Excavating a pit like Seth\_01 by sublimating ice on the wall and floor would take more than 7,000 years (Methods). The cylindrical shape of most pits also provides evidence against formation by erosion, because this would result in elongated shapes and a latitudinal dependence of the pit distribution on the surface.

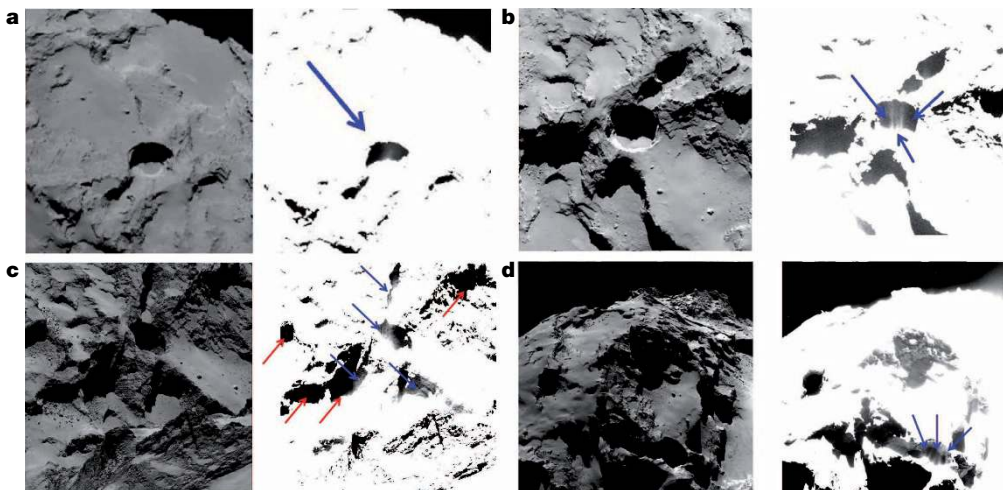


**Figure 2 | Jet-like features in the Seth region.** a–d, Views of the main active pit in the Seth region, at different angles of solar illumination. The illuminated area of the pit is the south wall (a), the north wall (b), the east wall (c) and the southeast wall (d). Blue arrows point to detected jets; red arrows indicate areas

where no activity could be observed, either from the walls or from their surroundings. The left images are the original data; the right images are linearly stretched in brightness to display the lowest 5% of the intensity values.

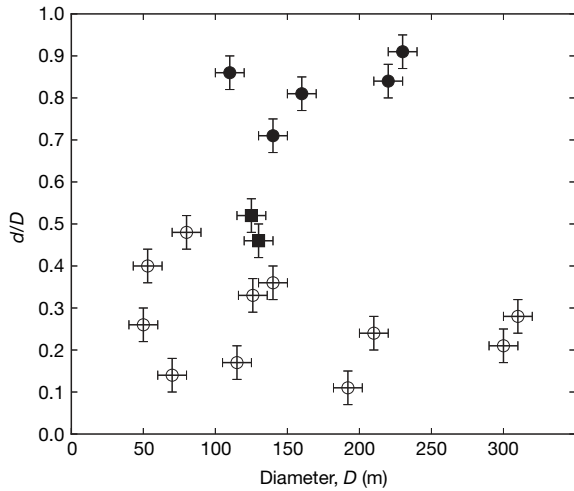


**Figure 3 | Depth-to-diameter ratio as a function of pit diameter.** Filled symbols describe active pits; empty symbols describe currently inactive pits. Filled circles are active pits in the Seth region; filled squares are active pits in the Ma'at region. The lower value of  $d/D$  for pits in the latter might indicate a different formation mechanism. Error bars represent the uncertainties inherent to the shape reconstruction technique (stereo-photogrammetry) used to produce the digital terrain model of the comet<sup>12</sup>.

The 380 pits observed on comet 9P have been associated with explosive activity<sup>9</sup>. In the weeks before its encounter with this comet, the spacecraft Deep Impact observed at least 10 outbursts, the largest of which ejected an estimated  $(6-30) \times 10^4$  kg of material<sup>10,15,16</sup>. The observations suggest that these outbursts originated from a series of pits located in a belt around the nucleus. At 4.11 AU from the Sun, on 30 April 2014, OSIRIS observed an outburst on comet 67P (ref. 17). Depending on the assumed size distribution of the ejected dust, the resulting plume contained  $10^3-10^5$  kg of material, and was thus of similar magnitude to the outbursts observed on comet 9P. Such outbursts are too small to create the observed pits by explosive excavation. Assuming a constant density<sup>12</sup> of  $470 \text{ kg m}^{-3}$ , a typical large active pit on comet 67P would have contained approximately  $10^9$  kg of material,  $10^4$  times more than the upper limit on the mass of the material excavated by the observed outburst.

We propose that the pits are formed via sinkhole collapse, when the ceiling of a subsurface cavity becomes too thin to support itself (Fig. 4 and Methods). Because the size of sinkholes depends on the material strength of the top layers, sinkholes in a given terrain are all of similar size. They are characterized by circular depressions aligned with the local gravity vector<sup>18</sup>.

On cometary nuclei, the removal of subsurface volatiles may generate a void. Failure of the cavity's ceiling propagates upward. From the observed pit diameters and depths, and by treating the cavity's roof as

an unsupported beam failing under its own weight, we estimate that the collapsing layer has an average tensile strength of 50 Pa (Extended Data Fig. 8 and Methods). This value is similar to the lower-limit estimate based on overhangs on the surface<sup>19</sup>. The collapse exposes fresh material in the walls of the pit, which sublimates to produce the observed jets. Such collapse may very well be the driver of the 30 April 2014 outburst from comet 67P and the mini-outbursts from comet 9P. The morphology and expansion of the dust plume of the 30 April 2014 outburst from comet 67P suggest that most of the activity arose from an area within  $30^\circ$  of latitude of the north pole<sup>17</sup>, compatible with the location of the pits in the Seth region.

The collapse itself is a sudden event, but the cavity 100–200 m below the surface could have been growing over a much longer timescale. We explore three cavity formation scenarios: (1) primordial voids inherited from formation; (2) direct sublimation of super volatiles (CO and CO<sub>2</sub>) as an evolutionary process; and (3) deep subsurface sublimation triggered by a secondary source of energy.

(1) The primordial scenario implies that voids existed in the nucleus since its formation. This is possible if the comet formed by slow accretion of cometsimals of tens to hundreds of metres in size. Low collision speeds would prevent crushing the cavities<sup>20</sup>. A weakening of the surface due to direct sublimation would trigger roof collapse.

(2) Cavity formation can also be an evolutionary process. Because comet nuclei have very low thermal conductivity<sup>21</sup>, direct sublimation of hexagonal water ice at the required depths would occur at an extremely low rate and can therefore be ruled out. It is possible, however, to sublimate more volatile ices like CO and CO<sub>2</sub> at lower temperatures. The fact that we do not see pits everywhere suggests that these super volatiles may not be distributed evenly inside the nucleus; such heterogeneity has been observed on the surface of other comets (9P, ref. 22; 103P, ref. 23).

(3) A subsurface energy source may provide the heat necessary to sublimate a large cavity. A candidate is the phase transition in water ice from an amorphous to a crystalline structure. Crystallization has been used to explain many cometary activity features, and has been suggested as the underlying process for the distant outbursts of comet 1P/Halley and the chaotic behaviour of comet 29P/Schwassmann–Wachmann<sup>24</sup>, or the outburst of comet 17P/Holmes<sup>25</sup>. Different models have placed the crystallization front at depths ranging from a few metres to hundreds of metres<sup>26,27</sup>. We find that a subsurface cavity of the size of the observed pits would require the phase transition of at least 600 kg of amorphous ice, corresponding to a sphere of 2 m in diameter at most (see Methods). The detailed calculation of the amount needed is beyond the scope of this Letter.

Ultimately, regardless of the process creating the initial subsurface cavity, active pits indicate that large structural and/or compositional heterogeneities exist within the first few hundred metres below the current nucleus surface of comet 67P. Clusters of active pits and collapsed structures are signatures of former cavities underneath, and reflect the thermal history of the nucleus.

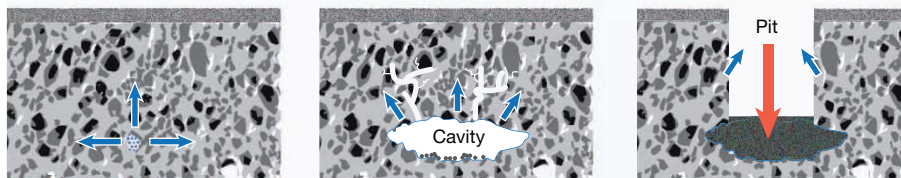


**Figure 4 | Pit formation mechanism by sinkhole collapse.** A typical comet surface with a layer of dust covering a mixture of dust and volatile material. A subsurface heat source sublimes surrounding ices. This gas then escapes or relocates, thus forming a cavity. When the ceiling becomes too thin to support

its own weight it collapses, creating a deep, circular pit with a smooth bottom. Newly exposed material in the pit's walls can start to sublimate. Blue arrows and white lines describe the escape of volatiles and fracturing of the surrounding material; red arrow shows the collapse of the cavity ceiling.

1. Keller, H. U., Kramm, R. & Thomas, N. Surface features on the nucleus of comet Halley. *Nature* **331**, 227–231 (1988).
2. Soderblom, L. A. *et al.* Observations of comet 19P/Borrelly by the miniature integrated camera and spectrometer aboard Deep Space 1. *Science* **296**, 1087–1091 (2002).
3. Brownlee, D. E. *et al.* Surface of young Jupiter family comet 81P/Wild 2: view from the Stardust spacecraft. *Science* **304**, 1764–1769 (2004).
4. Thomas, P. C. *et al.* The nucleus of comet 9P/Tempel 1: shape and geology from two flybys. *Icarus* **222**, 453–466 (2013).
5. A'Hearn, M. F. *et al.* Deep Impact: excavating comet Tempel 1. *Science* **310**, 258–264 (2005).
6. Schultz, P., Hermalyn, B. & Veverka, J. The Deep Impact crater on 9P/Tempel-1 from Stardust-NExT. *Icarus* **222**, 502–515 (2013).
7. Holsapple, K. A. & Housen, K. R. A crater and its ejecta: an interpretation of Deep Impact. *Icarus* **187**, 345–356 (2007).
8. Vincent, J.-B., Oklay, N., Marchi, S., Höfner, S. & Sierks, H. Craters on comets. *Planet. Space Sci.* **107**, 53–63 (2015).
9. Belton, M. J. S. *et al.* The origin of pits on 9P/Tempel 1 and the geologic signature of outbursts in Stardust-NExT images. *Icarus* **222**, 477–486 (2013).
10. Belton, M. J. S. *et al.* Cometary cryo-volcanism: source regions and a model for the UT 2005 June 14 and other mini-outbursts on comet 9P/Tempel 1. *Icarus* **198**, 189–207 (2008).
11. Keller, H. U. *et al.* OSIRIS – The scientific camera system onboard Rosetta. *Space Sci. Rev.* **128**, 433–506 (2007).
12. Sierks, H. *et al.* On the nucleus structure and activity of comet 67P/Churyumov-Gerasimenko. *Science* **347**, aaa1044 (2015).
13. Kirk, R. *et al.* Topography of the 81P/Wild 2 nucleus derived from Stardust stereoisimages. *Lunar Planet. Sci.* **XXXVI**, 2244 (2005).
14. Basilevsky, A. T. & Keller, H. U. Comet nuclei: morphology and implied processes of surface modification. *Planet. Space Sci.* **54**, 808–829 (2006).
15. Farnham, T. L. *et al.* Dust coma morphology in the Deep Impact images of comet 9P/Tempel 1. *Icarus* **187**, 26–40 (2007).
16. Feldman, P. D. *et al.* Hubble Space Telescope observations of comet 9P/Tempel 1 during the Deep Impact encounter. *Icarus* **187**, 113–122 (2007).
17. Tubiana, C. *et al.* 67P/Churyumov-Gerasimenko: activity between March and June 2014 as observed from Rosetta/OSIRIS. *Astron. Astrophys.* **573**, A62 (2015).
18. Waltham, T., Bell, F. G. & Culshaw, M. G. *Sinkholes and Subsidence* (Springer, 2007).
19. Thomas, N. *et al.* The morphological diversity of comet 67P/Churyumov-Gerasimenko. *Science* **347**, aaa0440 (2015).
20. Weissman, P. R., Asphaug, E. & Lowry, S. C. in *Comets II* (eds Festou, M. C. *et al.*) 337–357 (Univ. Arizona Press, 2004).
21. Groussin, O. *et al.* The temperature, thermal inertia, roughness and color of the nuclei of comets 103P/Hartley 2 and 9P/Tempel 1. *Icarus* **222**, 580–594 (2013).
22. Feaga, L. M., A'Hearn, M. F., Sunshine, J. M., Groussin, O. & Farnham, T. L. Asymmetries in the distribution of H<sub>2</sub>O and CO<sub>2</sub> in the inner coma of comet 9P/Tempel 1 as observed by Deep Impact. *Icarus* **190**, 345–356 (2007).
23. A'Hearn, M. F. *et al.* EPOXI at comet Hartley 2. *Science* **332**, 1396–1400 (2011).
24. Prialnik, D., Benkhoff, J. & Podolak, M. in *Comets II* (eds Festou, M. C. *et al.*) 359–387 (Univ. Arizona Press, 2004).
25. Hillman, Y. & Prialnik, D. A quasi 3-D model of an outburst pattern that explains the behavior of comet 17P/Holmes. *Icarus* **221**, 147–159 (2012).
26. Tancredi, G., Rickman, H. & Greenberg, J. M. Thermochemistry of cometary nuclei. I. The Jupiter family case. *Astron. Astrophys.* **286**, 659–682 (1994).
27. Marboeuf, U. & Schmitt, B. How to link the relative abundances of gas species in coma of comets to their initial chemical composition? *Icarus* **242**, 225–248 (2014).

**Acknowledgements** OSIRIS was built by a consortium of the Max-Planck-Institut für Sonnensystemforschung, Katlenburg-Lindau, Germany, the CISAS, University of Padova, Italy, the Laboratoire d'Astrophysique de Marseille, France, the Instituto de Astrofísica de Andalucía, CSIC, Granada, Spain, the Research and Scientific Support Department of the European Space Agency, Noordwijk, The Netherlands, the Instituto Nacional de Técnica Aeroespacial, Madrid, Spain, the Universidad Politécnica de Madrid, Spain, the Department of Physics and Astronomy of Uppsala University, Sweden, and the Institut für Datentechnik und Kommunikationsnetze der Technischen Universität Braunschweig, Germany. The support of the national funding agencies of Germany (DLR), France (CNES), Italy (ASI), Spain (MEC), Sweden (SNSB), and the ESA Technical Directorate is acknowledged. This work was also supported by NASA JPL contract 1267923 to the University of Maryland (M.F.A'H. and D.B.). M.F.A'H. is a Gauss Professor at the Akademie der Wissenschaften zu Göttingen and Max-Planck-Institut für Sonnensystemforschung (Germany). This research has made use of NASA's Astrophysics Data System Bibliographic Services. We thank H. J. Melosh for reviews and criticism.

**Author Contributions** J.-B.V. led the study, identified the pits and measured their global parameters. D.B. analysed outbursts and phase change transitions and prepared the sinkhole model. S.B. performed the detailed morphology analysis. H.S., C.B., P.L., R.R., D.K. and H.R. are the lead scientists of the OSIRIS project. The other authors are co-investigators who built and ran this instrument and made the observations possible, and associates and assistants who participated in the study.

**Author Information** All data presented in this paper will be delivered to the ESA's Planetary Science Archive and NASA's Planetary Data System in accordance with the schedule established by the Rosetta project and will be available on request before that archiving. Reprints and permissions information is available at [www.nature.com/reprints](http://www.nature.com/reprints). The authors declare no competing financial interests. Readers are welcome to comment on the online version of the paper. Correspondence and requests for materials should be addressed to J.-B.V. ([vincent@mps.mpg.de](mailto:vincent@mps.mpg.de)).



## METHODS

**Detection of activity.** Cometary activity is typically defined as the ensemble of physical processes forming the gas and dust coma that escapes from the nucleus. The main driver of activity is the solar insolation, which triggers the sublimation of volatiles trapped in the subsurface of the nucleus<sup>28</sup>. The liberated gas expands into vacuum and drags along refractory grains from the surface. It has been known since the first *in situ* mission to a comet that this activity is not uniformly distributed over the nucleus although the reasons for this anisotropy are not well understood<sup>1</sup>.

From the uneven distribution of active sources on the surface, anisotropies in the coma arise in the form of narrow dusty streams (hereafter called 'jets'), which expand straight from the nucleus for at least some distance<sup>29</sup>. Neither their source nor the physics of their formation have been fully explained yet, although many authors have proposed some explanations such as patches of enhanced H<sub>2</sub>O ice content, localized super-volatile release from steep-sided pits, or repetitive mini-outbursts<sup>30</sup>. It is not clear whether these features are linked to volatiles at their footprint or if they trace the shock front between competing gas flows from nearby areas<sup>31</sup>.

In OSIRIS images, jets appear as fuzzy streams of bright material arising from specific areas on the nucleus surface. They are typically detected against the coma or a dark background, which can be either empty space or cast shadows. They are seen at all spatial scales, from large features spanning several tens of kilometres, down to the limit of spatial resolution. The smallest features detected so far are a few pixels across, which translates into a couple of metres at most. Their typical surface brightness is 10% to 40% higher than the surrounding background space, that is, the general coma<sup>12</sup>. By monitoring the activity and observing these jets from different angles we can perform stereo imaging, reconstruct their three-dimensional structure and trace them back precisely to morphological features on the surface.

**Orbit integration.** Observations and orbit reconstructions have shown that comet 67P had a close encounter with Jupiter that brought its perihelion from 2.7 AU to 1.2 AU, in 1959 (JPL Horizons ephemerides, <http://ssd.jpl.nasa.gov/horizons.cgi>). We reconstructed its orbit before that time, on the basis of a well-established integration model<sup>32</sup>. For the initial conditions and their errors, we refer to the database of IMCCE (<http://www.imcce.fr/langues/en/ephemerides/>). We compute 200 clone orbits with random Gaussian small variations of the initial conditions considering their Gaussian errors. From these 200 clone orbits, we deduce the mean perihelion distance and its standard deviation ( $\sigma$ ). We find that 84% of the orbits in the interval  $[(\text{mean} - \sigma), (\text{mean} + \sigma)]$  and the orbits beyond  $(\text{mean} + \sigma)$  have a perihelion distance greater than at least 2 AU with a mean value always greater than 3 AU (Extended Data Fig. 1).

**Morphology, variegation and activity of the pits.** The pit morphologies are presented in more detail in Extended Data Figs 3, 4. The complete list of OSIRIS images used for this study is given in Extended Data Table 2.

The activity identified in Seth\_01 covers the portion of the pit presented in Fig. 1, which displays different morphologies and textures. Therefore, it is not clear at this point that a specific texture and morphology is linked to the active pits. The detailed observations of the pits Ma'at\_01 and Ma'at\_02 seem to indicate that heavily fractured terrains are, however, favourably associated with activity. Extended Data Fig. 3 highlights the multiple joints that are also associated with the globular texture for Ma'at\_01. Thus, fractured texture might be favourable for these active pits, probably because it allows the heat to propagate deeper into the interior and sublimate the ices. One other possible location for the activity inside the pits could be the terraces seen in Seth\_01 (and maybe in Ma'at\_02, although they are less developed). The two terraces highlighted in Extended Data Fig. 3 cover around 50% of the circumference of the Seth\_01 pit, and they match the 50% where activity has been identified so far. Therefore, the terraces could be the source of the activity if they expose some kind of fresh ice (or gas/ice from the coma falling back and depositing on this flat surface).

The contact between the edges of the pits and the surroundings is different between the active pits Seth\_01 and Ma'at\_01. This could be the result of different mechanisms that formed them or the primordial morphology of the region. The bottoms of most pits are covered with a fine dusty material and boulders, which could be an indication of the relative age of these pits. Seth\_01's floor appears very flat (Extended Data Figs 3, 4), with a very smooth structure that does not contain any boulders. The floors of Seth\_02 and Seth\_03, pits where activity has been identified, share the same textural characteristics as Seth\_01. The viewing conditions are less favourable for Ma'at\_01; however, Extended Data Figs 3–5 show few boulders, all of small size. The same figures highlight that Ma'at\_02 has a much higher number of boulders with larger sizes. These boulders may be an indirect way of estimating the relative age of the pits, because boulders accumulate with time. Thus, boulder-free floors represent the youngest pits. The relative age dating of these pits could also be speculated from the Ma'at\_01 to Ma'at\_03 series of pits.

With Ma'at\_01 being the youngest and Ma'at\_03 the oldest, one can see the degradation of the wall of the pits and the accumulation of material within the pit. The accumulation of boulders is rather limited in Ma'at\_03, although the degradation of the rim is in a more advanced stage when compared to the other two, which confirms that it is the oldest. This low accumulation could be due to the geometry of Ma'at\_03 or related to the original depth of the pit, which is most likely to have been smaller. The boulder-size distributions in the Seth and Ma'at pits are shown in Extended Data Figs 5, 6.

We used additional images obtained through filters near the visible spectrum (blue: 480 nm, orange: 649 nm, infrared: 989 nm) to see if, in addition to the peculiar morphology, pits present a different colour to the rest of the surface. By using filter ratios to limit the effect of topography and illumination conditions, we found that the floor and walls of the pits exhibit the same less-red spectral slope as the active Hapi region (Extended Data Fig. 7). If we denote the reflectance by  $R$ , then we measure a ratio  $R_{\text{infrared}}/R_{\text{blue}} = 1.8$  in the active area (pits) and  $R_{\text{infrared}}/R_{\text{blue}} = 2.1$  elsewhere on the nucleus. A full understanding of the implications of the compositional differences within the nucleus will require a dedicated investigation, but the difference in spectral slope observed in Extended Data Fig. 7 already indicates that spectral variation is an intrinsic property of currently active regions on comet 67P.

**Pit growth.** A major question is whether the  $d/D$  ratio of the pits can be explained by the current sublimation-driven retreat of the walls. We see jets arising from the edges of active pits (Fig. 1), indicating that erosion currently does occur. We first consider slowly excavating a pit by sublimating subsurface ice on the walls and floor and growing the depressions in both diameter and depth. We take as an example the most active pit (Seth\_01). With a diameter of 220 m and a depth of 185 m, it has a volume of  $7 \times 10^9 \text{ m}^3$ , which corresponds to  $3.3 \times 10^9 \text{ kg}$  of material if we assume a constant density of  $470 \text{ kg m}^{-3}$ . Current models of activity for comet 67P (refs 33–35) describe a global dust production rate of  $9.3 \text{ kg s}^{-1}$  at 3.5 AU, which translates into only  $15 \text{ g s}^{-1}$  of dust emitted from a single pit. Additionally, the varying latitudes and seasons limit the pits' illumination to only a few hours per comet day for the walls. In some cases, the pit floor is only barely illuminated, if at all. Considering that most currently observed pits will be in polar night at perihelion and will not experience many changes in dust production rate, it would take more than 7,000 years to dig out one pit.

Erosion is a second-order process that will slowly modify the pits after they are formed. This is supported by our observations; several active pits display alcoves within their walls, which we interpret as signatures of continued growth as a result of erosion by sublimation, block falls and wall retreats long after the pit formation, because these alcoves are always facing the direction of most insolation received per comet rotation.

**Phase transition.** Crystallization has been invoked to explain many cometary activity features, and has been suggested as the underlying process for the distant outbursts of comet 1P/Halley<sup>24</sup>, the chaotic behaviour of comet 29P/Schwassmann-Wachmann<sup>24</sup> and the violent outburst of comet 17P/Holmes<sup>25</sup>.

From the ratio between the latent heat of the amorphous-to-crystalline transition ( $9 \times 10^4 \text{ J kg}^{-1}$ , refs 36, 37) and of the sublimation of hexagonal ice ( $0.334 \text{ J kg}^{-1}$ ), the phase transition of 1 kg of amorphous ice to crystalline ice provides enough energy to sublimate 270 kg of hexagonal ice, provided that crystallization occurs on a timescale short enough for the phase transition to effectively heat the surrounding ice. Using typical low thermal inertia, Marboeuf and Schmitt<sup>28</sup> find that crystallization proceeds to a depth of only approximately 1 m. Other studies estimate that the crystallization front should extend to depths of between about 5 m and about 80 m (ref. 37), or much greater depths<sup>27</sup>.

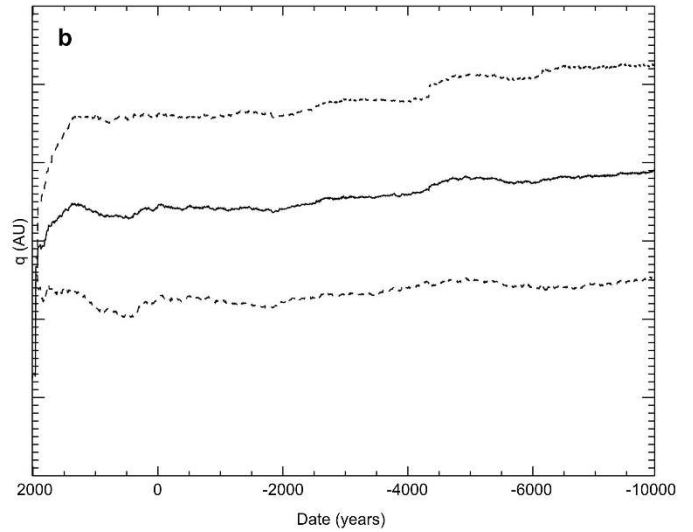
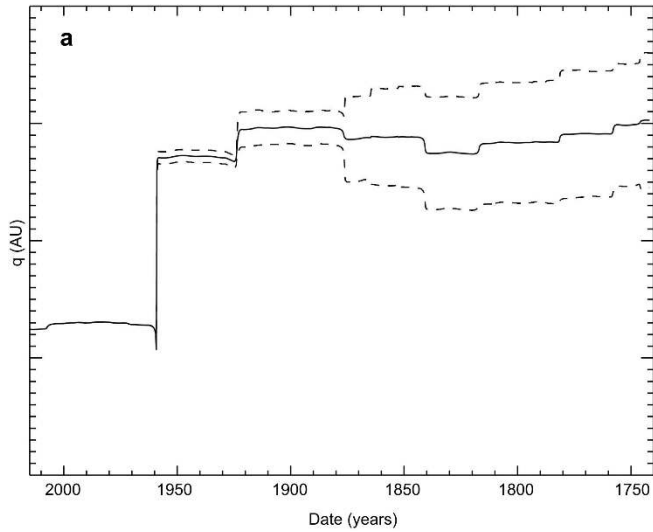
Given the chaotic orbital evolution of comet 67P, we estimate that a 100 m deep layer could have recently reached the appropriate characteristics (100–120 K leading to a phase transition on a timescale of months to a year) only if the local thermal inertia is high ( $250 \text{ J m}^{-2} \text{ K}^{-1} \text{ s}^{-1/2}$  and above), a value more than five times what has been measured on comet 67P. For lower values of the thermal inertia, the phase transition can occur at a depth of 100–200 m only after a long period of time in the inner Solar System. A cavity could have formed much earlier in the history of the comet, even if the final collapse that produced the observed sinkhole occurred only recently. A subsurface cavity the size of the pits we observe would require the phase transition of approximately 600 kg of amorphous ice to crystalline ice. If we assume a density of  $470 \text{ kg m}^{-3}$  and a porosity of 70–80%, we obtain a 20–40% ice mass fraction in the nucleus (ice density is  $920 \text{ kg m}^{-3}$ , solid material is half silicate and half organics, with respective densities of  $3,500 \text{ kg m}^{-3}$  and  $2,200 \text{ kg m}^{-3}$ ). Therefore, 600 kg of ice would be embedded in 1,500–3,000 kg of cometary material and would occupy a volume of 3–6 m<sup>3</sup>, that is, a sphere of at most 2 m in diameter. Upon experiencing its phase transition, this pocket of amorphous ice would release enough heat to sublimate the surrounding crystalline ice in a volume equivalent to the observed pits.

**Sinkhole model.** A first order estimate of the stability of a cavity ceiling may be derived by treating the ceiling a beam failing under its own weight<sup>18,38</sup>. Failure of this beam occurs when the bending moment exceeds the material's tensile strength. Assuming the comet's material is highly porous, the stable beam depth  $d = 6D^2\rho a/(8S)$ , where  $D$  is the cavity's diameter,  $\rho$  is the density of the material in the ceiling (assumed to be  $470 \text{ kg m}^{-3}$ ),  $a$  is the gravitational acceleration on the comet<sup>12</sup> ( $5 \times 10^{-4} \text{ m s}^{-2}$ ) and  $S$  is the tensile strength of the ceiling material. For the tensile strength, we adopted an initial range between the lower limit of 10 Pa derived from overhangs on the surface<sup>19</sup> and the upper limit of 10 kPa derived from the Deep Impact experiment<sup>39</sup>. We further assume that the cavity is of approximately the same size as the resulting pit and that the depth of the pit is comparable to the depth of the original ceiling.

**Code availability.** The code used to generate the orbital evolution of comet 67P is a direct implementation of a published model<sup>32</sup>.

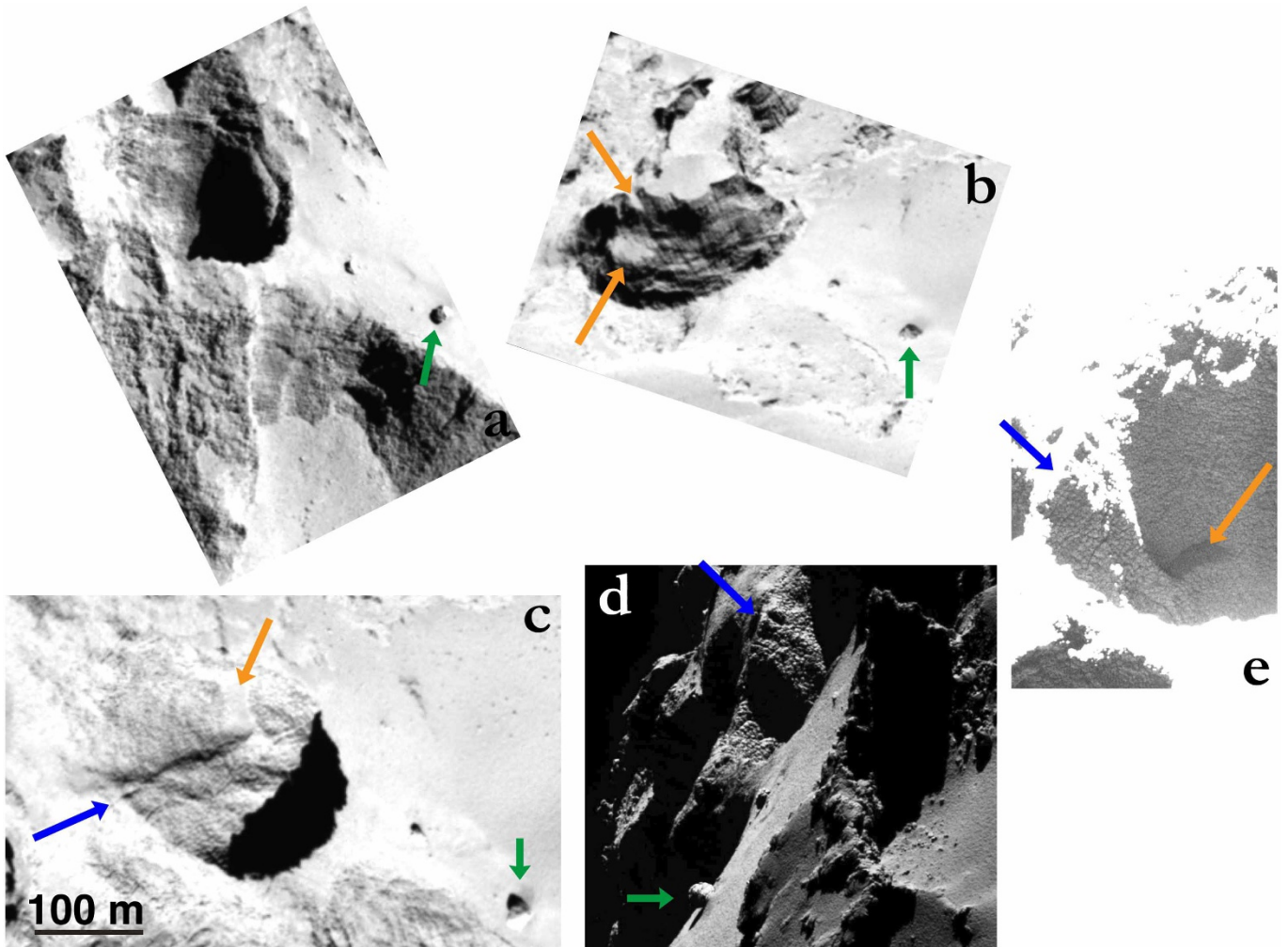
28. Delsemme, A. H. in *Comets* (ed. Wilkening, L. L.) 85–130 (Univ. Arizona Press, 1982).
29. Sekanina, Z. Anisotropic emission from comets: fans versus jets. I. Concept and modeling. In *Proc. International Symposium on the Diversity and Similarity of Comets*, Vol. ESA SP-278, 315–322 (1987).
30. Belton, M. J. S. Cometary activity, active areas, and a mechanism for collimated outflows on 1P, 9P, 19P, and 81P. *Icarus* **210**, 881–897 (2010).

31. Crifo, J.-F., Rodionov, A. V., Szegő, K. & Fulle, M. Challenging a paradigm: do we need active and inactive areas to account for near-nuclear jet activity? *Earth Moon Planets* **90**, 227–238 (2002).
32. Marsden, B. G., Sekanina, Z. & Yeomans, D. K. Comets and non-gravitational forces. *V. Astron. J.* **78**, 211–225 (1973).
33. Tozzi, G. P. *et al.* Evolution of the dust coma in comet 67P/Churyumov-Gerasimenko before the 2009 perihelion. *Astron. Astrophys.* **531**, A54 (2011).
34. Lara, L. M., Lin, Z.-Y., Rodrigo, R. & Ip, W.-H. 67P/Churyumov-Gerasimenko activity evolution during its last perihelion before the Rosetta encounter. *Astron. Astrophys.* **525**, A36 (2011).
35. Snodgrass, C. *et al.* Beginning of activity in 67P/Churyumov-Gerasimenko and predictions for 2014–2015. *Astron. Astrophys.* **557**, A33 (2013).
36. Ghormley, J. A. Enthalpy changes and heat-capacity changes in the transformations from high-surface-area amorphous ice to stable hexagonal ice. *J. Chem. Phys.* **48**, 503–508 (1968).
37. De Sanctis, M. C., Lasue, J. & Capria, M. T. Seasonal effects on comet nuclei evolution: activity, internal structure, and dust mantle formation. *Astron. J.* **140**, 1–13 (2010).
38. White, W. B. *Geomorphology and Hydrology of Karst Terrains* (Oxford Univ. Press, 1988).
39. Richardson, J. E. & Melosh, H. J. An examination of the Deep Impact collision site on comet Tempel 1 via Stardust-NExT: placing further constraints on cometary surface properties. *Icarus* **222**, 492–501 (2013).



**Extended Data Figure 1 | Perihelion distance of comet 67P as a function of time.** Solid line, mean value of the orbits integrated according to a Monte Carlo method. Dashed lines, standard deviation of the mean value. **a**, Perihelion

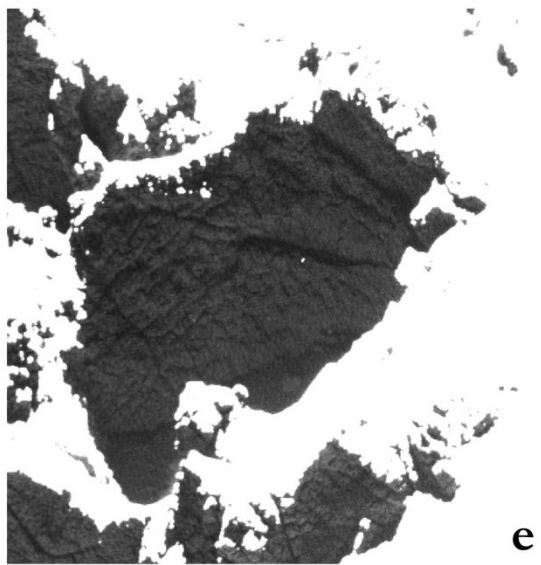
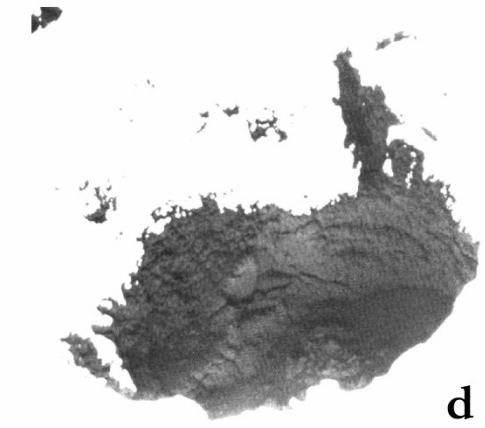
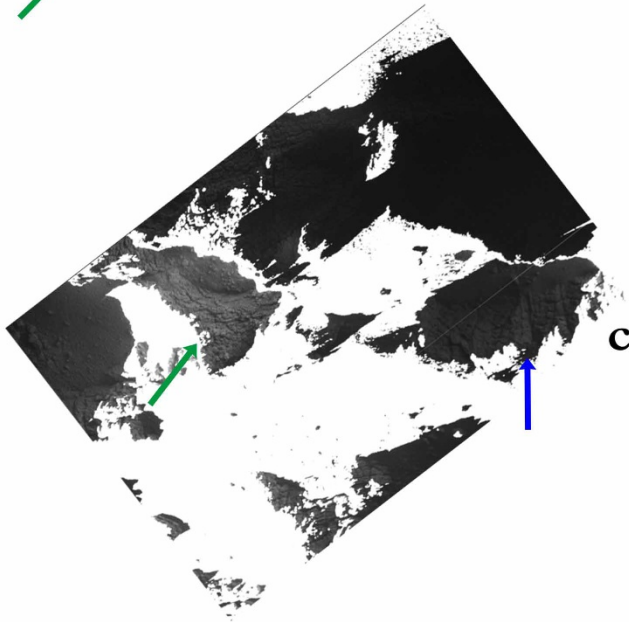
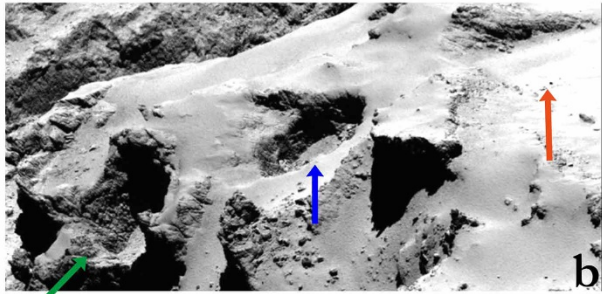
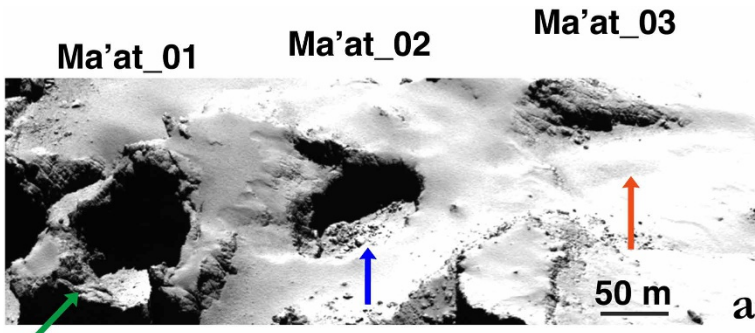
distance over the last 270 years, when comet 67P experienced several close encounters with Jupiter. **b**, The long term integration over the full dynamical lifetime of the comet (10,000 years).



**Extended Data Figure 2 | Multiple views of the Seth\_01 pit observed by the OSIRIS camera.** **a**, Southern part of the pit wall; **b**, western part of the pit wall; **c**, **d**, eastern part of the pit wall with different illumination conditions; and **e**, southeastern part of the pit wall observed in the shadow. In all the images, the

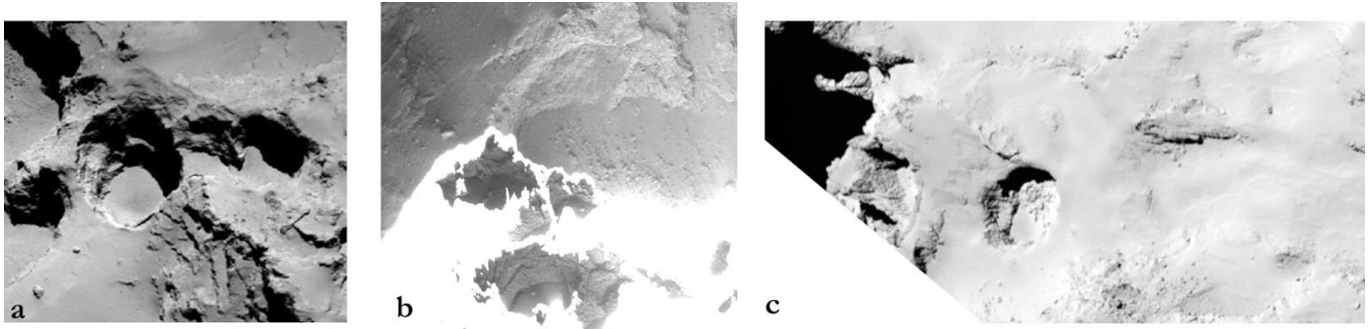
green arrow points to the same boulder and the blue arrow to the same ridge inside the pit. The orange arrows point to terraces within the pit. The Seth\_01 pit is 220 m in diameter.





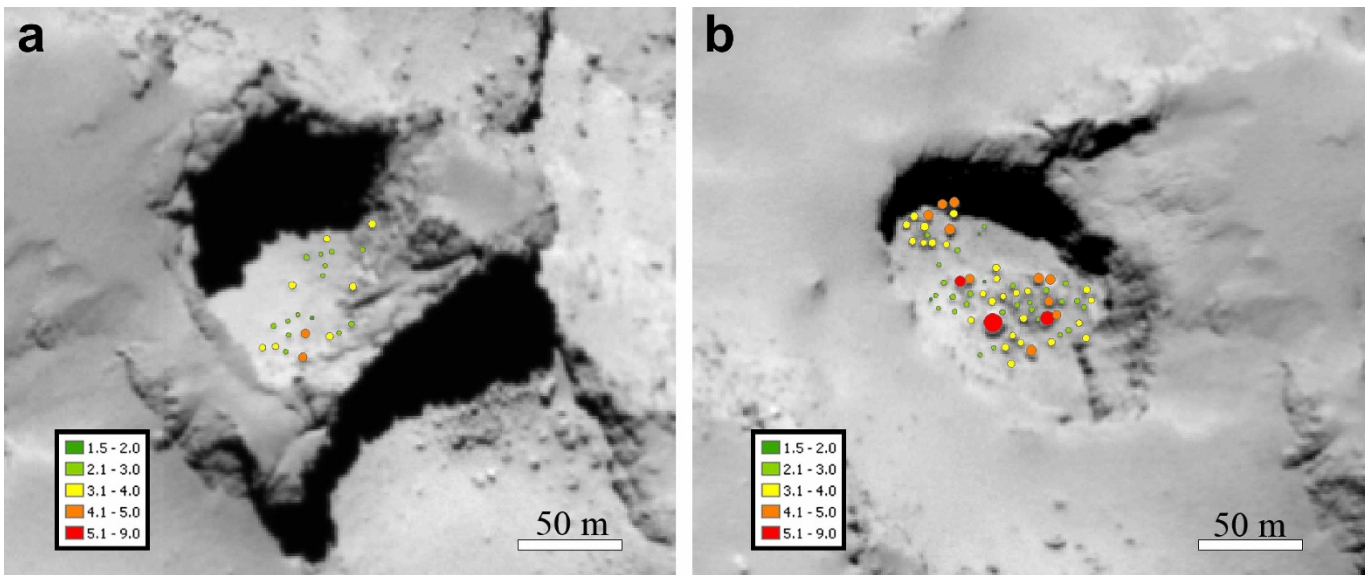
**Extended Data Figure 3 | Multiple views of the Ma'at\_01, Ma'at\_02 and Ma'at\_03 pits observed by the OSIRIS camera. a, b,** Side views of the pits with different illumination conditions; **c,** opposite viewing conditions highlighting the other side in the shadow; and **d, e,** detailed views of Ma'at\_02 (**d**) and Ma'at\_01 (**e**) from light reflection in the shadow. Note the clear cross-cutting

fractures on the wall in **e**. In **c**, the white line is an artefact due to stretching of the image to highlight the shadowed part. The Ma'at\_02 pit is 130 m in diameter. The blue, green and oranges arrows point to the same features in each image.



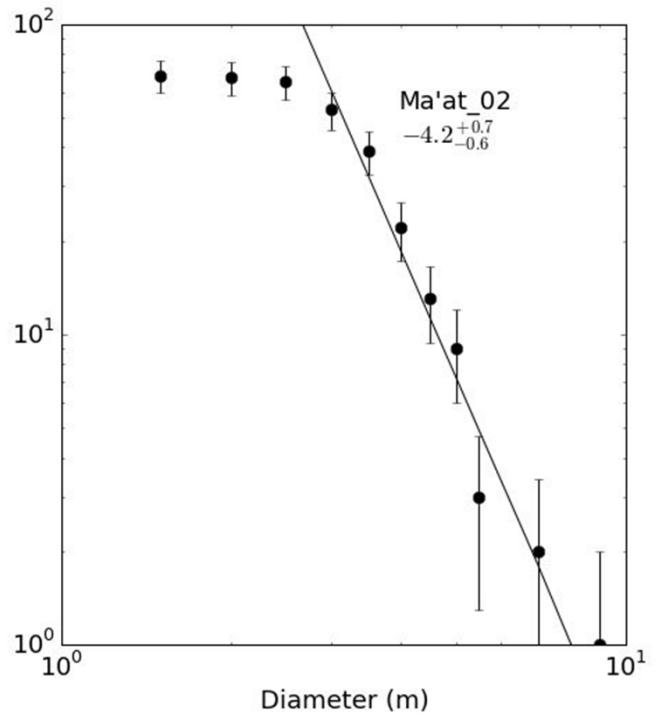
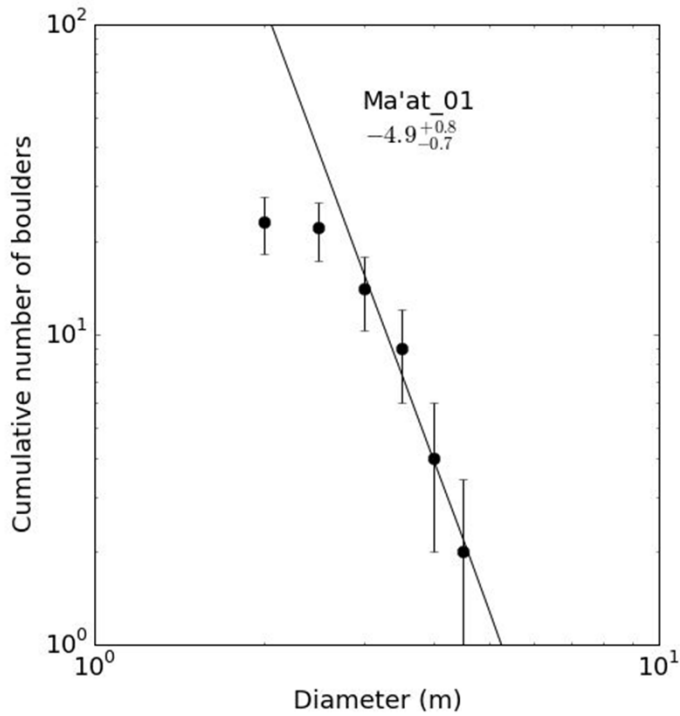
**Extended Data Figure 4 | Additional views of the Seth\_01 and Ma'at\_01 pits.** **a**, The floor of Seth\_01 shows no accumulation of boulders; the same is true for Seth\_02 and Seth\_03 (not shown). **b**, The floor of Ma'at\_01 shows a few

boulders that have accumulated; note the activity located at the bottom. **c**, The floor of Ma'at\_02 shows an asymmetric accumulation of boulders that could be the result of upper wall collapse.



**Extended Data Figure 5 | Boulder counts in Ma'at\_01 and Ma'at\_02.** We counted boulders on the floor of Ma'at\_01 and Ma'at\_02. We used OSIRIS narrow angle camera (NAC) images with a resolution of 1.2 metres per pixel, acquired at 67 km from the comet nucleus centre. **a**, **b**, The illumination conditions are such that almost 80% of the floor of Ma'at\_01 (**a**) and 95% of the floor of Ma'at\_02 (**b**) are illuminated and the pits are facing the observer, which ensures an unbiased boulder count. We identified 23 boulders inside

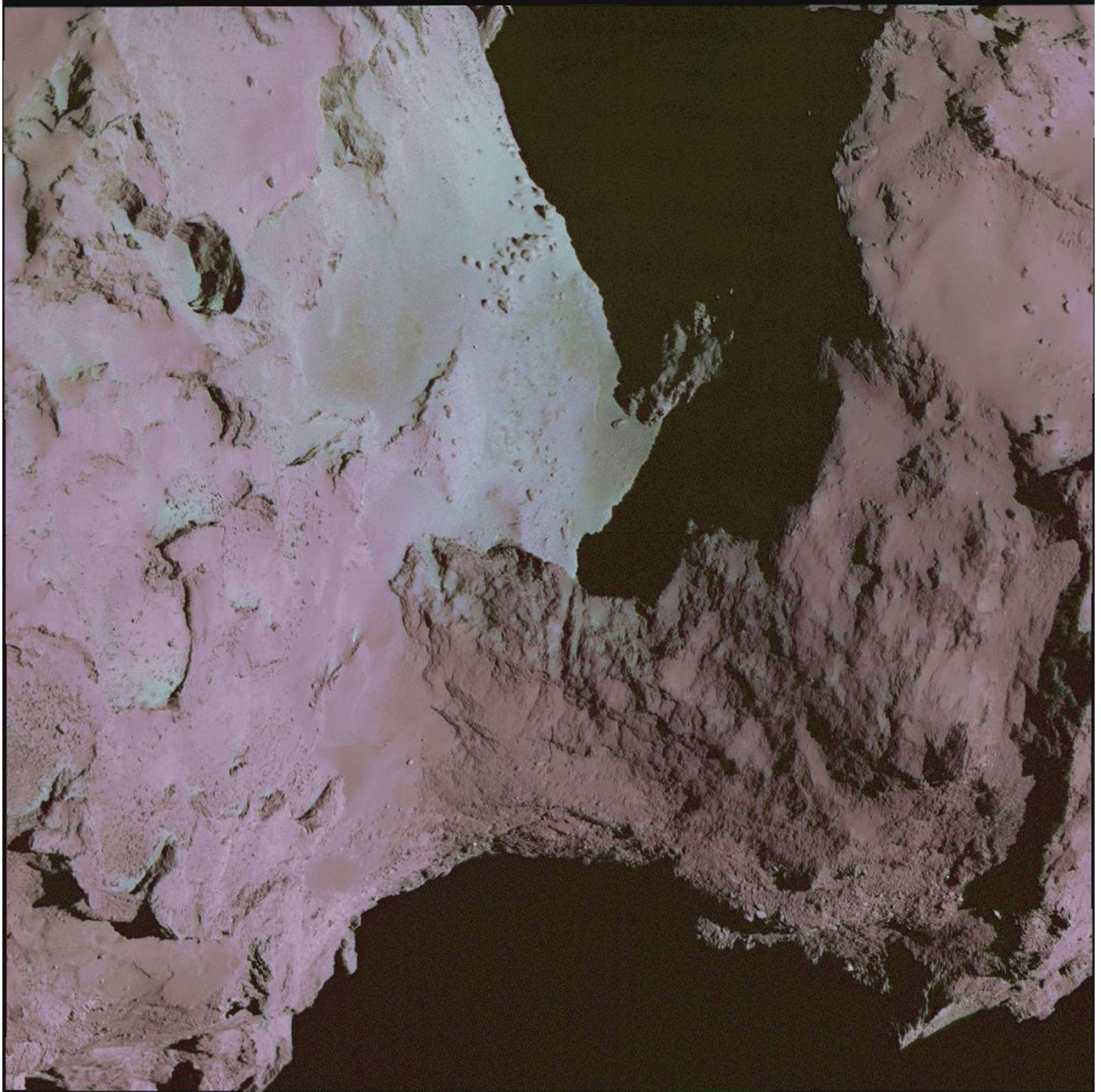
Ma'at\_01 and 68 on the floor of Ma'at\_02. The diameter of the boulders (in metres) is indicated by the coloured circles; see inset. Despite the 1.2 metres per pixel resolution, we were able to identify some boulders with a diameter between 1.5 m and 2.5 m (9 in Ma'at\_01 and 15 in Ma'at\_02), owing to the presence of elongated shadows. The maximum boulder diameter is 4.3 m in Ma'at\_01 and 9.0 m in Ma'at\_02.



**Extended Data Figure 6 | Cumulative boulder-size distribution for Ma'at\_01 and Ma'at\_02.** This distribution has a power index of  $-4.9^{+0.8}_{-0.7}$  for Ma'at\_01 (left) and  $-4.2^{+0.7}_{-0.6}$  for Ma'at\_02 (right), for boulder diameters greater than 3 m; the corresponding power laws are indicated the by the solid (fit) lines. Boulders smaller than 3 m in diameter are at the edge of our detection limit, meaning that the counts for these boulders are less reliable than the other

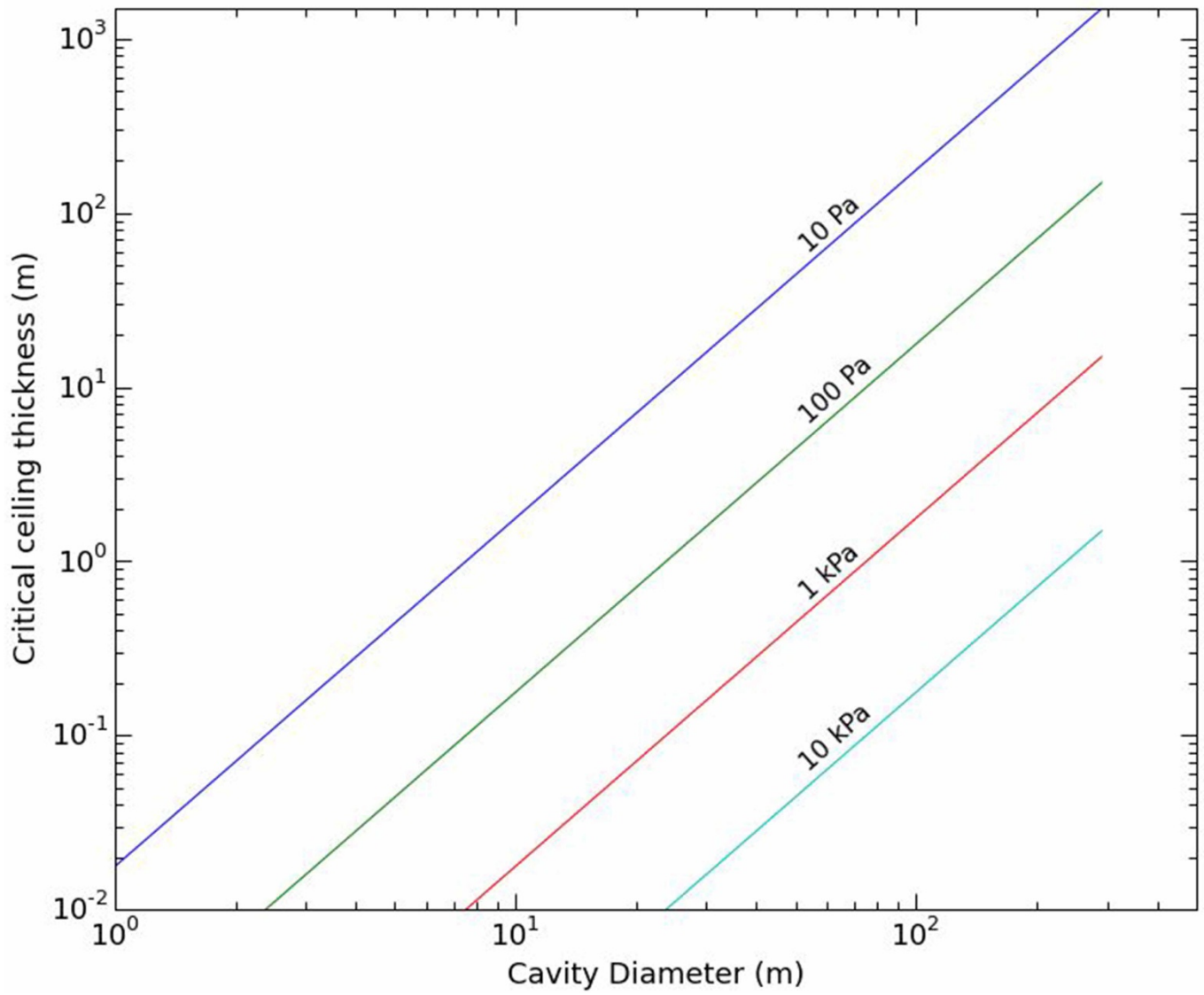
counts; consequently, they were not included when fitting the power law. The higher number of boulders in Ma'at\_02 is consistent with the theory that boulders are debris that falls from the walls as the pit erodes, long after the initial formation of the pit. Error bars are defined as the square root of the cumulative number of boulders to reflect the increasing diameter uncertainty for small boulder sizes.





**Extended Data Figure 7 | RGB view of the Seth pits and the Hapi region.** The red–blue–green components of this colour map represent colour ratios between the reflectance signals measured at different wavelengths: red, 989 nm/649 nm; green, 480 nm/649 nm; blue, 649 nm. The colour map is overlaid

onto a grey image showing the comet surface. The Hapi region and part of Seth appear with a blue hue, indicative of a bluer spectral slope than other regions of the nucleus, which are typically red. The interior of Seth\_01, Seth\_02 and Seth\_03 have the same blue hue that is characteristic of the active Hapi region.



**Extended Data Figure 8 | Modelled critical ceiling thickness for increasing cavity diameter and different tensile strengths.** We predict the average tensile strength of a collapsed layer using the dimensions of a pit (Methods). For

example, a pit of 220 m in diameter and 185 m in depth (such as, Seth\_01) suggests that the collapsed layer had an average tensile strength of 50 Pa.



Extended Data Table 1 | List of pits considered in this paper

| Pit Id    | Latitude (°) | Longitude (°) | Diameter (m) | Depth (m) | d/D  | Jets detected? |
|-----------|--------------|---------------|--------------|-----------|------|----------------|
| Seth_01   | 70           | 220           | 220          | 185       | 0.84 | Yes            |
| Seth_02   | 69           | 205           | 110          | 95        | 0.87 | Yes            |
| Seth_03   | 68           | 195           | 140          | 100       | 0.72 | Yes            |
| Seth_04   | 78           | 198           | 160          | 130       | 0.77 | Yes            |
| Seth_05   | 57           | 239           | 230          | 210       | 0.92 | Yes            |
| Seth_06   | 39           | 204           | 210          | 50        | 0.24 | No             |
| Ash_01    | 30           | 90            | 70           | 10        | 0.14 | No             |
| Ash_02    | 36           | 85            | 50           | 13        | 0.26 | No             |
| Ash_03    | 23           | 204           | 126          | 42        | 0.33 | No             |
| Ash_04    | 20           | 210           | 192          | 21        | 0.11 | No             |
| Ash_05    | 20           | 216           | 300          | 64        | 0.21 | No             |
| Ash_06    | 23           | 226           | 310          | 87        | 0.28 | No             |
| Ma'at_01  | 42           | 8             | 125          | 65        | 0.52 | Yes            |
| Ma'at_02  | 35           | 9             | 130          | 60        | 0.47 | Yes            |
| Ma'at_03  | 35           | 2             | 140          | 50        | 0.37 | No             |
| Ma'at_04  | -10          | 327           | 115          | 20        | 0.18 | No             |
| Bastet_01 | 3            | 21            | 80           | 38        | 0.48 | No             |
| Hathor_01 | 25           | 26            | 53           | 21        | 0.40 | No             |

Diameter and depth measured on digital terrain model reconstructed from OSIRIS images by stereo-photogrammetry<sup>12</sup>. Active pits have a mean  $d/D = 0.73 \pm 0.08$ ; inactive pits have a mean  $d/D = 0.26 \pm 0.08$ . Maximum error is 20 m for the diameter and 5 m for the depth. Coordinates are given in the 'Cheops' reference frame<sup>12</sup>.

Extended Data Table 2 | List of images used

| <b>Pits in Seth region</b>                       | <b>Distance from nucleus center (km)</b> | <b>Resolution on the surface (m/px)</b> |
|--|--|---|
| NAC_2014-08-06T02.19.14.570Z_ID30_1397549900_F22 | 119.2                                    | 2.18                                    |
| NAC_2014-08-21T11.42.53.641Z_ID30_1397549800_F22 | 72.6                                     | 1.31                                    |
| NAC_2014-08-21T13.42.54.561Z_ID30_1397549200_F22 | 72.95                                    | 1.31                                    |
| NAC_2014-08-28T20.42.53.590Z_ID30_1397549900_F22 | 56.24                                    | 1.00                                    |
| NAC_2014-08-29T04.42.56.583Z_ID30_1397549200_F22 | 54.90                                    | 0.98                                    |
| NAC_2014-08-29T20.42.53.538Z_ID00_1397549900_F22 | 56.06                                    | 1.00                                    |
| NAC_2014-09-02T21.44.22.575Z_ID30_1397549800_F22 | 64.16                                    | 1.15                                    |
| NAC_2014-09-20T01.48.48.382Z_ID30_1397549200_F22 | 28.2                                     | 0.48                                    |
| NAC_2014-10-02T00.26.22.560Z_ID30_1397549300_F22 | 20.65                                    | 0.34                                    |
| NAC_2014-10-02T12.11.26.599Z_ID30_1397549700_F22 | 20.86                                    | 0.35                                    |
| NAC_2014-10-03T13.40.22.589Z_ID30_1397549900_F22 | 21.18                                    | 0.36                                    |
| WAC_2014-10-20T08.15.50.752Z_ID30_1397549000_F18 | 9.2                                      | 0.73                                    |

| <b>Pits in Ma'at region</b>                      | <b>Distance from nucleus center (km)</b> | <b>Resolution on the surface (m/px)</b> |
|--|--|---|
| NAC_2014-08-21T20.42.54.581Z_ID30_1397549100_F22 | 67.04                                    | 1.21                                    |
| NAC_2014-08-21T21.42.54.553Z_ID30_1397549300_F22 | 66.54                                    | 1.20                                    |
| NAC_2014-08-22T21.41.54.592Z_ID00_1397549000_F22 | 60.14                                    | 1.08                                    |
| NAC_2014-09-12T01.33.04.375Z_ID30_1397549400_F22 | 27.55                                    | 0.48                                    |
| WAC_2014-09-12T04.10.28.751Z_ID30_1397549100_F17 | 27.57                                    | 2.63                                    |
| NAC_2014-09-13T03.36.12.463Z_ID30_1397549200_F22 | 30.05                                    | 0.52                                    |
| NAC_2014-10-03T17.37.22.649Z_ID30_1397549100_F22 | 19.19                                    | 0.32                                    |
| NAC_2014-10-04T05.27.21.576Z_ID30_1397549100_F22 | 19.19                                    | 0.32                                    |
| NAC_2014-10-14T21.40.03.314Z_ID30_1397549700_F22 | 10.57                                    | 0.16                                    |
| WAC_2014-10-20T04.52.10.460Z_ID10_1397549600_F18 | 9.31                                     | 0.75                                    |

Also shown is the distance from the comet nucleus centre that the image was taken and the resolution of the image.